

# Ice Rule Breakdown and frustrated antiferrotoroidicity in an artificial colloidal Cairo ice

**Carolina Rodríguez-Gallo<sup>1,2</sup>, Antonio Ortiz-Ambriz<sup>1,3</sup>, Cristiano Nisoli<sup>4</sup>, and Pietro Tierno<sup>1,2,5</sup>**

<sup>1</sup>Departament de Física de la Matèria Condensada, Universitat de Barcelona, 08028, Barcelona, Spain.

<sup>2</sup>Universitat de Barcelona Institute of Complex Systems (UBICS), Universitat de Barcelona, 08028 Spain.

<sup>3</sup>Tecnologico de Monterrey, Escuela de Ingeniería y Ciencias, Campus Monterrey, 64849 Mexico.

<sup>4</sup>Los Alamos National Laboratory, Los Alamos, NM 87545, United States of America.

<sup>5</sup>Institut de Nanociència i Nanotecnologia, Universitat de Barcelona, 08028 Spain.

E-mail: [ptierno@ub.edu](mailto:ptierno@ub.edu)

*Keywords:* Geometric Frustration, colloids, magnetism, chirality

**Abstract.** We combine experiments and numerical simulations to investigate the low energy states and the emergence of topological defects in an artificial colloidal ice in the Cairo geometry. This type of geometry is characterized by a mixed coordination ( $z$ ), with coexistence of both  $z = 3$  and  $z = 4$  vertices. We realize this particle ice by confining field tunable paramagnetic colloidal particles within a lattice of topographic double wells at a one to one filling using optical tweezers. By raising the interaction strength via an applied magnetic field, we find that the ice rule breaks down, and positive monopoles with charge  $q = +2$  accumulate in the  $z = 4$  vertices and are screened by negative ones ( $q = -1$ ) in the  $z = 3$ . The resulting, strongly coupled state remains disordered. Further, via analysis of the mean chirality associated to each pentagonal plaquette, we find that the disordered ensemble for this geometry is massively degenerate and it corresponds to a frustrated antiferrotoroid.

## 1. Introduction

The Cairo geometry is a type of Euclidean plane tiling made of a sequence of connected pentagons which share vertices with two types of coordination numbers, namely  $z = 3$  and  $z = 4$  [1, 2]. Besides its aesthetic beauty, as testified by the presence of the Cairo geometry in numerous artistic paintings and pavements, especially in Egypt [3], such lattice is also important in frustrated spin systems. For example, it has been experimentally found in different magnetic compounds such as the  $\text{Bi}_2\text{Fe}_4\text{O}_9$  [4] and the  $\text{Bi}_4\text{Fe}_5\text{O}_{13}\text{F}$  [5], apart from being the subject of theoretical studies on Ising-type models [6–9]. Recently, such geometry has been considered as an interesting way to organize interacting dipolar nanoislands on a plane, also known as artificial spin ice systems (ASIs) [10–12]. ASIs are lattice of ferromagnetic elements that interact via in-plane dipoles and are arranged to produce geometric frustration effects [13–20]. In the Cairo geometry, recent experimental works have found a rich behavior due to frustration [21, 22], while Monte Carlo simulations reported the presence of long-range order [23]. Even mechanical analogues of Cairo artificial spin ice were realized via 3D-printing [24].

Particle ice systems are soft matter analogues of ASIs but based on interacting colloids constrained to move within a lattice of double wells [25, 26]. In contrast to ASIs that feature in-plane dipoles, the colloidal particles present out-of-plane, induced dipoles and pair interactions that can be tuned by an external field. The microscopic size of the particles allows the use of optical microscopy to visualize their dynamics and thus, to extract all relevant degrees of freedom. The particle ice was originally proposed with a set of double wells generated optically [25, 27], while experiments were realized by using lithographically patterned substrates [28–30]. Moreover, it was shown theoretically that, for a lattice of single coordination number  $z$ , the colloidal ice is analogous to an ASI since the low energy states fulfill similar ice-rules, i.e. minimization of the associated topological charge [31]. Such similarity however, breaks down for lattices of mixed coordination such as decimated systems [32]. Indeed, in a colloidal ice, particles at a vertex tend to repel each other, and therefore the single vertex energy is different from

ASI. If we consider the colloid as a token of a topological charge, then each vertex wants to push away as much charge as possible. In certain geometries this is impossible and the same trade-off, corresponding to the ice rule, is realized on each vertex. Thus, the colloidal ice for an extended, single coordinated lattice behaves as a spin ice [31, 33]. In other cases that is not true [32], as we show below for the Cairo geometry, and a transfer of topological charge takes place between vertices of different coordination, breaking the ice rule.

This fact underlines that particle based ice offers the possibility of investigating a rich set of physical phenomena, different than ASIs [30, 33–35]. And indeed many other recent realizations testify to the broader phenomenology of particle-based systems as models for geometric frustration. These include confined microgel particles [36–40], mechanical metamaterials [41–46], patterned superconductors [47, 48], skyrmions in liquid crystals [49, 50] and interacting macroscopic rods [51, 52].

In this article we experimentally realize a Cairo colloidal ice by confining repulsive paramagnetic colloidal particles within a lattice of lithographic double wells, as shown in Fig. 1(a). To place and move these particles within the topographic traps, we use a modified set of laser tweezers that generate an optical ring rather than a focalized spot. This strategy allows to easily trap and move paramagnetic particles, avoiding heating due to absorbed light. By investigating the low energy states, we find that topological charges can accumulate in different sublattices, breaking locally the ice rules. We complement our finding with Brownian dynamic simulations, which show good agreement with the experimental data in terms of fraction of vertices, topological charges and net chirality associated to each pentagonal plaquette of the Cairo lattice. Finally we perform simulations on an extended system to calculate chirality correlation functions and to elucidate the system frustration at high field strength.

## 2. The artificial colloidal ice

The schematic in Fig. 1(b) and the optical microscope image in Fig. 1(c) illustrates the basic features of a Cairo colloidal ice. The system presents a lattice of lithographic elliptical traps composed of two wells of lateral elevation  $h \sim 3\mu\text{m}$  that are connected by a small central hill. These wells are filled with paramagnetic colloidal particles of diameter  $d = 10\mu\text{m}$  and magnetic volume susceptibility  $\kappa = 0.025$ . A particle of volume  $V = \pi d^3/6$  has to overcome a gravitational potential  $U_g = \Delta\rho Vgh \sim 2000\text{ k}_B\text{T}$  to jump outside the double well due to thermal fluctuations. Here  $\Delta\rho = \rho_p - \rho_w \sim 0.6\text{ g cm}^{-3}$  is the difference between the mass density of the particle ( $\rho_p$ ) and the dispersing medium ( $\rho_w$ ). Thus, the particles are essentially confined within the elliptical traps and cannot change their location from one well to another unless subjected to an external force, such as the repulsion from a neighboring colloid. We induce such repulsion by applying an external magnetic field  $\mathbf{B}$  perpendicular to the sample pane, Fig. 1(b). Once the field is applied, each particle acquires an induced dipole moment  $\mathbf{m} = V\kappa\mathbf{B}/\mu_0$ , being  $\mu_0$  the permeability of the medium. Thus, a pair of particles ( $i, j$ ) placed at a relative distance

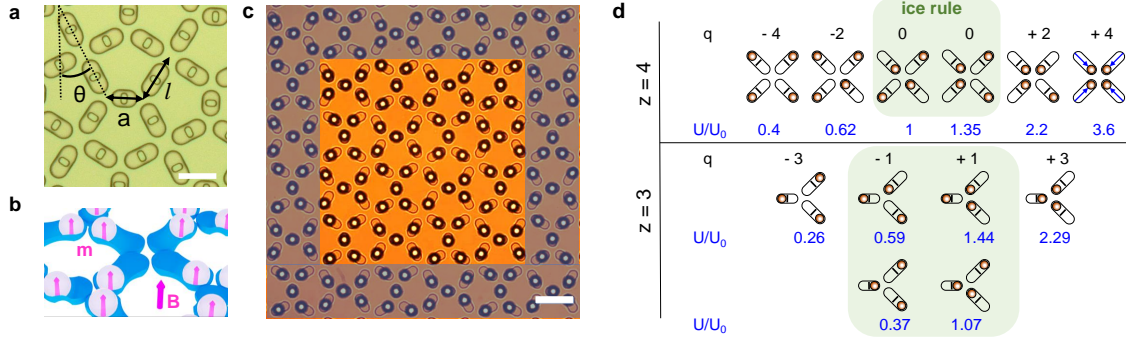


**Figure 1.** (a) Image of a lithographic structure made of double wells and arranged along the Cairo geometry with the different parameters overlaid:  $\theta$  is the bond angle,  $a$  is the distance between two  $z = 3$  vertices,  $l$  between  $z = 3$  and  $z = 4$  vertices; scale bar is  $10 \mu\text{m}$ . (b) Schematic showing the double wells filled with paramagnetic colloidal particles. The external field  $\mathbf{B}$  induces an equal dipole moment  $\mathbf{m}$  in each particle. (c) Experimental realization of a Cairo colloidal ice, where the colloidal particles appear as black disks. The shaded gray region excludes vertices from the statistical analysis, in order to minimize effects due to open boundaries. Scale bar is  $20 \mu\text{m}$ . (d) Different configurations with corresponding topological charges  $q$  (black) and rescaled total energy  $U/U_0$  (blue) for vertices of coordination  $z = 4$  (top row) and  $z = 3$  (bottom row). Here  $U_0 = 6.2k_B T$  is the energy of the ground state vertex in the  $z = 4$  for a field of  $B = 10 \text{ mT}$ . The last vertex in the  $z = 4$  illustrates the Ising-like spins associated to each double well. The green box shows the vertices obeying the ice rules for the coordination  $z = 4$  ( $q = 0$ ) and  $z = 3$  ( $q = \pm 1$ ).

$r = |\mathbf{r}_i - \mathbf{r}_j|$  experience a repulsive dipolar interaction which is isotropic and inversely proportional to  $r^3$ ,  $U_{dd} = \mu_0 m^2 / (4\pi r^3)$ . This interaction potential can be tuned via the applied field and, for an amplitude of  $B = 10 \text{ mT}$ ,  $U_{dd} = 122 k_B T$  ( $U_{dd} = 4.7 k_B T$ ) for the closest (farthest) distance of  $r = 13 \mu\text{m}$  between two particles in a  $z = 3$  vertex ( $r = 38.4 \mu\text{m}$  in a  $z = 4$  resp.).

The mapping between the colloidal ice and an ASI [25] can be obtained by assigning an Ising-like spin to each double well, such that it points where the particle is located Fig. 1(d). Using this mapping, one can distinguish between different type of vertices depending on the lattice coordination. For example, for the  $z = 4$  (square lattice) there are 6 possible arrangements of the particles with different energetic weights, while for the  $z = 3$  (honeycomb lattice) these reduce to 4. Moreover, in analogy to the ASI, one can assign a topological charge to each vertex defined here as  $q = 2n - z$  being  $n$  the number of spins that point toward the vertex center. Note that we can talk of topological charges when considering the vertices within a lattice, not isolated ones. By this notion of charge, an extended lattice is overall charge-neutral, and thus charges appear in pair and disappear only when annihilated by other defects in order to guarantee the charge conservation,  $\sum q_i = 0$ . For example, the vertex with four colloids pointing outwards ( $q = -4$ ) is characterized by the lowest energetic weight of the  $z = 4$ , and thus, when considered alone it will be the natural state of repulsive colloids. However, within a

lattice the  $q = -4$  is topologically connected to the  $q = +4$  due to particle conservation and thus they are unlikely to occur. One can prove that in a lattice, lower absolute values of the topological charges  $|q| = 0, 1$ , corresponding to the ice-rule, are favored [33]. Indeed the ice rules, highlighted by the green box in Figure 1(d) are a prescription of the minimization of  $|q|$ , given by vertices with  $q = 0$  for  $z = 4$  and  $q = \pm 1$  for  $z = 3$ .

Regarding the Cairo geometry, we have a mixture of  $z = 4$  and  $z = 3$  vertices, the latter characterized by unequal lengths of the double wells, as shown in Fig. 1(d). Upon analysis of the total magnetic interaction energy of a vertex  $U$ , we find that the  $z = 4$  vertices have same energy hierarchy as the square colloidal ice investigated in previous works [28, 29]. Here  $U = \sum_{i=1}^{N_v-1} \sum_{j=i+1}^{N_v} U_{ij}^{dd}$ , being  $N_v$  the number of particles in a vertex. However, the presence of the small double well in the  $z = 3$  vertices, i.e. a length of  $4.53 \mu\text{m}$  while in the  $z = 4$  is  $10 \mu\text{m}$ , induces an energetic spitting of the vertices 1-in-2-out and 2-in-1-out depending on the location of the paramagnetic colloid. This energy difference between the  $z = 3$  vertices, which does not affect the associated topological charge, is particular of the Cairo geometry, and it is not present in the  $z = 3$  vertices of the classical honeycomb [53, 54] and triangular [55] colloidal ice, where all traps have the same length. Even if the energy difference is relatively small, as we will show later this will induce a disordered ground state.

### 3. Experimental methods

The Cairo lattice is realized via soft-lithography using Polydimethylsiloxane (PDMS). This substrate was first designed using a commercial software (AutoCad, Adobe) and fabricated above a 5-inch soda-lime glass covered with a 500nm Chromium (Cr) layer. The chosen geometric parameters, as shown in Fig. 1(a), are  $a = 19.54 \mu\text{m}$ ,  $l = 26.7 \mu\text{m}$  and  $\theta = 30^\circ$ . We use laser lithography (DWL 66, Heidelberg Instruments Mikrotechnik GmbH) to write the double wells on the substrate with a 405nm laser diode working at a speed of  $5.7 \text{ mm}^2 \text{ min}^{-1}$ . After that, we replicate the double wells of the Cr mask in the PDMS following two steps. In the first one we duplicate the structure using an epoxy-based negative photoresist (SU-8) on top of a silicon wafer. Then we covered the structure with liquid PDMS by spinning the sample at 4000 rpm during 1 min with an angular speed of 2000 rpm (Spinner Ws-650Sz, Laurell). With this process we obtain a layer of  $\approx 20 \mu\text{m}$  thickness. The PDMS is solidified by baking for 30 min at  $95^\circ\text{C}$  in a leveled hot plate. After solidification of the PDMS, we peel off the structure with the help of a cover glass (MENZEL-GLASER, Deckglaser). The resulting sample is  $\sim 170 \mu\text{m}$  thick, and enough transparent to visible light.

Once fabricated, the sample is placed on the stage of an inverted optical microscope (TiU, Nikon) which is connected to a complementary metal oxide semiconductor camera (MQ013CG-E2, Ximea) able to record videos of the particle dynamics at 30Hz. The microscope is equipped with a  $40\times$  oil immersion objective (Nikon, numerical aperture 1.3) which is used both for observation and optical trapping purpose.

One microscope port is modified in order to accommodate an incoming beam

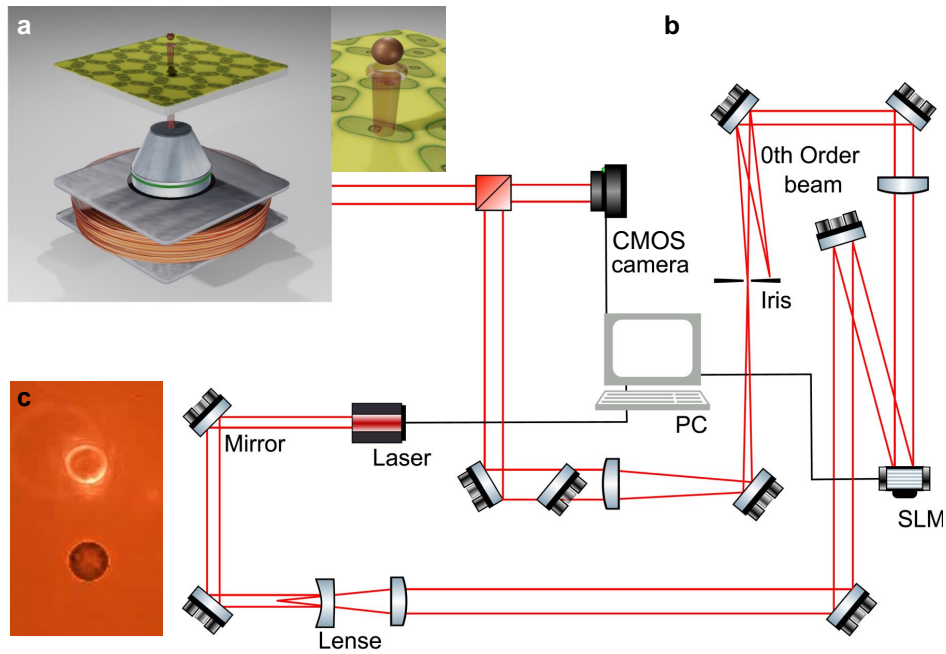


**Figure 2.** (a) Schematic showing a colloidal particle trapped above the topographic substrate by laser tweezers. The beam is focused with a microscope objective that passes through a magnetic coil. Side image shows an enlargement of the particle and the optical ring. (b) Detailed sketch of the experimental system illustrating the different optical components to send a near-infrared laser beam onto a spatial light modulator (SLM), and the system dynamics are visualized via a complementary metal oxide semiconductor (CMOS) camera. (c) Microscope image of a particle and the corresponding optical ring.

generated by a butterfly laser diode (wavelength  $\lambda = 976\text{nm}$ , operated at a power of  $70\text{mW}$ , BL976-SAG300 Thorlabs). The optical path of the laser is composed of a series of optical lenses including a spatial light modulator (SLM, Hamamatsu X10468-03) which is commanded by a LCOS-SLM controller (Hamamatsu), Figs. 2(a,b). The holograms are generated with a custom made Labview program.

The SLM is used to generate holographic optical tweezers (HOTs) which are composed of 4 lenses. The first two constitute a telescope and have focal lengths  $f = -75\text{ mm}$  (Thorlabs LC 1582-B) and  $f = 175\text{ mm}$  (Thorlabs LA 1229-B), respectively. After the SLM there is another telescope with a lens of focal  $f = 500\text{ mm}$  (Thorlabs LA1908-B) which focuses the beam after being deflected in order to filter the 0 mode via a diaphragm, and reaching a final lens of  $f = 750\text{ mm}$  (Thorlabs LA 1727-C), as shown in the detailed diagram of Fig. 2(b). Due to the optical absorption of the particles used, which are highly doped with nanoscale iron oxide grains ( $\sim 20\%$  by w.), we have implemented a novel strategy to trap the colloids without damaging them due to the generated heat. Instead of using a single focalized spot, we program the SLM such that the deflected beam generates an optical ring as shown in Figs. 2(a,c).

The external magnetic field was generated via a custom made coil located below

the sample. The magnetic coil is powered by an amplifier (BOP-20 10M, KEPCO), that is computer controlled using a digital analogue card (NI 9269) with a custom made LabVIEW program. The field was applied via a ramp at a rate  $0.05 \text{ mTs}^{-1}$  until reaching a maximum value of  $10 \text{ mT}$ .

#### 4. Numerical simulation

We complement the experiments performing Brownian dynamics simulations using as input parameters the experimental data. In particular, we use Euler's method to integrate the overdamped equations of motion for each colloidal particle  $i$  at position  $\mathbf{r}_i$ :

$$\gamma \frac{d\mathbf{r}_i}{dt} = \mathbf{F}_i^T + \mathbf{F}_i^{\text{dd}} + \boldsymbol{\eta} \text{ ,} \quad (1)$$

being  $\gamma = 0.033 \text{ pNs m}^{-1}$  the friction coefficient. Further terms in Eq. 1 are the force from the topographic double well  $\mathbf{F}_i^T$  which is modeled as a piece-wise harmonic bistable potential,

$$\mathbf{F}_i^T = -\mathbf{e}_\perp k R_\perp + \mathbf{e}_\parallel \delta \text{ .} \quad (2)$$

Here  $(\mathbf{e}_\parallel, \mathbf{e}_\perp)$  are unit vectors oriented parallel and perpendicular with respect to the line of length  $L$  that joins the two minima in the double well, whose associated vector is  $\mathbf{R} \equiv (R_\parallel, R_\perp)$ . Moreover  $\delta = \xi_1 R_\parallel$  if  $|R_\parallel| \leq \frac{\delta}{2}$  and  $\delta = k(\frac{L}{2} - |R_\parallel|)\text{sign}(R_\parallel)$  otherwise. As stiffness we use  $k = 1 \cdot 10^{-4} \text{ pN/nm}$  which keeps the particle confined to the elongated region around the center of the trap, and  $\xi_1 = 3 \text{ pN/nm}$  that creates a potential hill equivalent to the gravitational hill within the double wells.

The dipolar force on a particle  $i$  is given by,

$$\mathbf{F}_i^{\text{dd}} = \frac{3\mu_0}{4\pi} \sum_{j \neq i} \frac{\mathbf{m}^2 \hat{r}_{ij}}{|r_{ij}|^4} \text{ ,} \quad (3)$$

being  $\mu_0 = 4\pi \times 10^{-7} \text{ H/m}$  and  $\hat{r}_{ij} = (\mathbf{r}_i - \mathbf{r}_j)/|\mathbf{r}_i - \mathbf{r}_j|$ . Dipolar interactions are calculated in an iterative form such that the global field  $\mathbf{B}$  includes also that generated by all other dipoles. Moreover, we apply a large cut-off of  $200 \mu\text{m}$  to consider the effect of long range dipolar interactions.

Finally the last term in Eq. 1 is a random force characterized by a zero mean,  $\langle \boldsymbol{\eta} \rangle = 0$  and delta correlated,  $\langle \boldsymbol{\eta}(t) \boldsymbol{\eta}(t') \rangle = 2k_B T \gamma \delta(t - t')$ , being  $k_B$  the Boltzmann constant and  $T = 300 \text{ K}$  the ambient temperature.

To reproduce the experimental results we start by solving Eq. 1 with  $N_1 = 180$  particles which are arranged along  $3 \times 3$  unit cells and open boundary conditions, similar to Fig. 1(c). However, to consider a larger system when measuring the chirality correlation functions, we extend the simulations also to  $N_2 = 2000$  particles, where 800 are arranged along the  $z = 3$  vertices and 400 in the  $z = 4$ . This situation corresponds to a colloidal ice of  $10 \times 10$  unit cells also with open boundary conditions. To avoid that most of the particles in the  $z = 3$  vertices localize on top of the topographic hills, due to strong dipolar forces, we also reduce the particle magnetic susceptibility to  $\kappa_2 = 0.005$

and raise the spring constant of the central hill to  $\xi_2 = 25\text{pN/nm}$ . In all cases, we numerically integrate the equation of motion using a time step of  $\Delta t = 0.01\text{s}$ .

## 5. Measurements of the topological charges.

We start our experiments by first randomly placing the particles with the optical ring within the double wells according to a random number generator. In the initial, random configuration the highly charged monopoles  $q = \pm 4$  are the 10% of the total vertices,  $q = \pm 3$  are the 15%, while the 25% of vertices corresponds to low charged  $q = \pm 2$ , the rest is leave to the ice rule vertices. Then, we slowly raise the applied field with a ramp of  $0.05\text{mT s}^{-1}$ . Fig. 3(a) shows the evolution of the fraction of topological charges as classified in Fig. 1(d), for the Cairo ice. By increasing  $B$ , we find that already after  $B \sim 3\text{mT}$ , the fraction of high topological charges  $q = \pm 4$  in the  $z = 4$  and  $q = \pm 3$  in the  $z = 3$  vertices reduces almost to zero in favor of the low charged ones. In particular, vertices obeying the ice selection rules in the  $z = 4$  rise up to the 50%, being only overcome by the  $q = -1$  in the  $z = 3$  ( $\sim 60\%$ ), while the  $q = +1$  reduces to  $\sim 50\%$ . This reduction is accompanied by a slight increase of the charged monopoles  $q = +2$  and a decrease of the  $q = -2$ .

Crucially, Fig. 3(b) plots the average topological charge ( $\bar{q} = \frac{1}{N_z} \sum q_{z_i}$   $N_z$  being the number of vertices  $z$ ) for vertices of coordination 3 and 4. It shows a net separation of topological charges between vertices of different coordination, and thus charge transfer between sublattices, breaking the ice rule. Thus, while the total topological charge is conserved, or  $\sum q = 0$ , at the sublattice level we observe a transfer of topological charges as the field reaches  $B = 8\text{mT}$ . A net fraction of positive monopoles accumulate in the  $z = 4$  vertices, while the  $z = 3$  vertices are, on average, negatively charged. Note also the relatively good agreement between experimental data (open symbols) and numerical simulations (continuous lines), which are plot together in both graphs, while small deviations fall within the experimental/simulation error bars.

Importantly, charge transfer effect between sublattices does not occur in an ASI, whose ice rule is instead robust in most geometries as it is inscribed into the energetics of the vertices. It only occurs in a colloidal ice with mixed coordination geometry as the Cairo. This effect results from the different nature of geometric frustration in ASI and in the colloidal system [31]. While both systems display similar behavior in terms of vertex fraction for single coordination lattices, in a mixed coordination geometry the difference at the single vertex level emerges: repulsive colloids cannot emulate in-plane ferromagnetic spins as in ASI, and topological charges tend to redistribute in order to minimize the system energy.

While charge transfer and ice-rule fragility had been predicted [31] and experimentally verified [32] in a decimated square ice, the sign of the effect in the Cairo lattice is inverted. In Ref. [32], negative monopoles form on the  $z = 4$ , breaking the ice rule. In that case the  $z = 3$  vertices, which unlike the  $z = 4$  vertices are charged even when obeying the ice rule because of their odd coordination, do not violate the ice rule



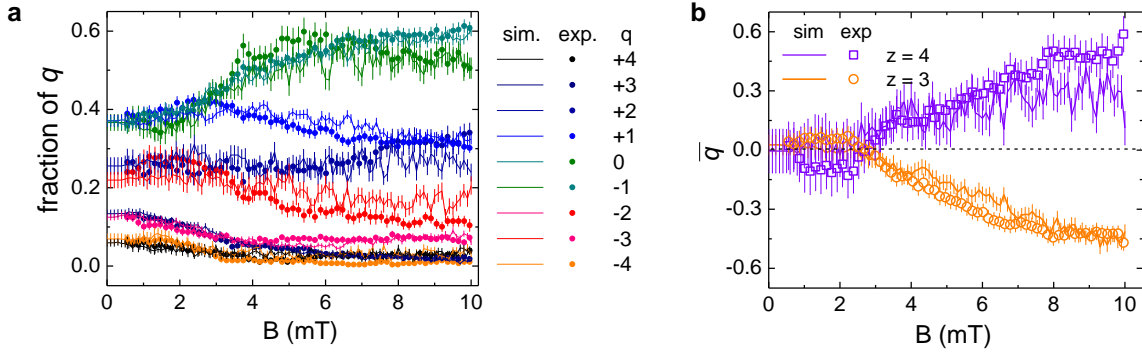


**Figure 3.** (a) Fraction of topological charges  $q$  for all vertex types (legend on left), and (b) mean topological charge  $\bar{q}$  for  $z = 3$  (empty circles) and  $z = 4$  (filled squares) vertices versus applied field strength  $B$ . In both graphs the symbols are experimental data, while the lines are results from numerical simulations.

but screen the negative charge of the  $z = 4$  vertices by changing their relative admixture of  $\pm 1$  charges, and thus assuming a net positive charge. In the Cairo system instead, the mechanism is similar but the sign of the charges is inverted. This is because Cairo is structurally different from a decimated square, with shorter and longer traps and thus a more complex energetics, as shown in Fig. 1(d). This allows also for structural transitions in the sign of the transferred charge as Cairo is deformed, and which we study elsewhere, while here we focus on the Cairo geometry.

### 5.1. Frustrated antiferrotoroidicity in the Cairo system

To better characterize the disorder of the charge-unbalanced, low-energy state of strongly-interacting Cairo colloidal ice, we study the chirality value, or associated toroidal moment, to each pentagonal plaquette. As shown in the inset in Fig. 4(a), this moment acquires a maximum value of  $\chi = -1$  (+1) for a full counter clockwise (clockwise) cell. Two natural questions are, firstly whether the plaquettes are naturally chiral, and secondly what is the mutual arrangement of these chiralities. To answer the first question, note that for a single pentagonal plaquette, a configuration that is fully chiral obeys the ice rule, that we know breaks down at high fields. At the same time, the long range interactions among colloids in further neighboring traps favors chirality. In the Cairo geometry the plaquette chirality is also favored by the asymmetry in the vertices of coordination  $z = 3$ . Because the traps between two of these vertices are considerably shorter than the others, moving these colloids *in*, i.e. towards the vertex center, it leads to a smaller change in energy than moving colloids along the longer traps. Thus, the particles in the two longer traps prefer to stay head-to-toe which gives a contribution  $2/5$  to chirality. However, those longer traps impinge on vertices of coordination  $z = 4$ . Assuming that they preferentially are in an antiferromagnetic configuration, as shown in the third image in Fig 4(a), that adds

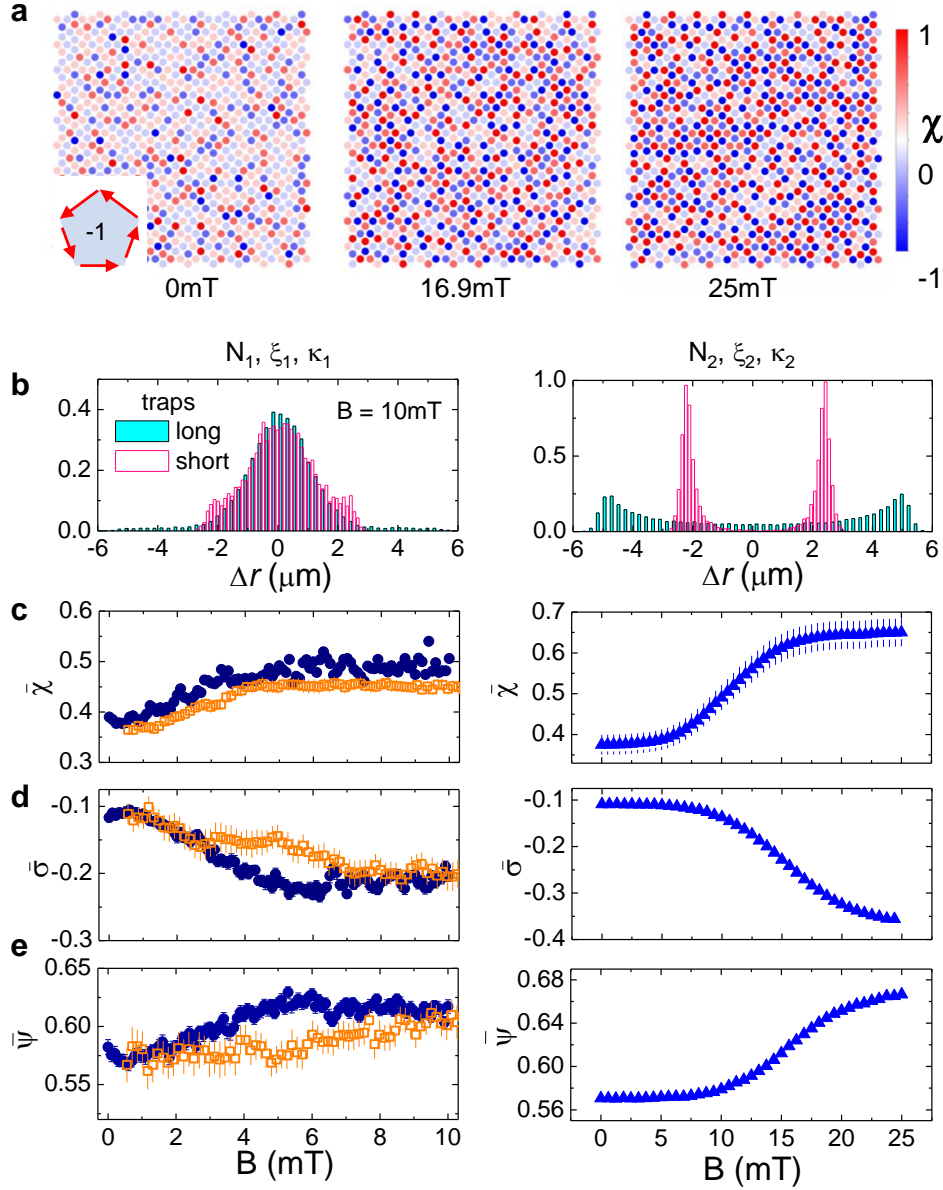


**Figure 4.** (a) Colormaps at different field amplitudes showing the evolution of the chirality  $\chi$  associated to each pentagonal plaquette for a system of 100 plaquettes. Small inset at the bottom of the first image illustrates a counter clockwise plaquette with  $\chi = -1$ . (b-e) Different panels correspond to two system size and parameters for simulations: left column  $N_1 = 180$  particles,  $\xi_1 = 3 \text{ pN nm}^{-1}$  and  $\kappa_1 = 0.025$  right column  $N_2 = 2000$  particles,  $\xi_2 = 25 \text{ pN nm}^{-1}$  and  $\kappa_2 = 0.005$ . In the first row (b) are the Histograms of positions of colloidal particles in the long (cyan) and short (pink) traps. Second (c) the mean chirality  $\bar{\chi}$ , third (d) the correlation  $\bar{\sigma}$  (d) and fourth (e) row the correlation  $\bar{\Psi}$  all versus applied magnetic field  $B$ . In all graphs on the left column, orange squares indicate experimental data while navy disk simulation one obtained for a 10 vertex lattice. Blue triangles on the right graphs are simulation results for a 100 vertex lattice.

another  $2/5$  contribution to the chirality for a total of  $\chi = 0.8$ .

Thus we expect that at large field strengths, the average absolute chirality of the systems,  $\bar{\chi} = \frac{1}{N_{pl}} \sum_i |\chi_i|$  being  $N_{pl}$  the number of plaquette, would tend towards  $\bar{\chi} \rightarrow 0.8$ . However we found that this was not the case, as shown in Fig 4(c), where both experiments and simulations show that at the largest applied field  $\bar{\chi} \sim 0.5$ . This lower value was due to the fact that, in the Cairo geometry, the magnetic colloids were found to locate above the central hill at the largest field amplitude,  $B = 10\text{mT}$ . Indeed this effect is shown in the first graph in Fig 4(b), where histograms of the particle positions from the simulations are reported for both the long and short double wells in the Cairo geometry. In this situation, since the trap bistability is lost, it is difficult to extract an accurate determination of  $\bar{\chi}$ .

To circumvent this problem numerically, we have performed further simulations using a larger system size and stronger confinement, i.e. increasing the hill spring constant from  $\xi_1 \rightarrow \xi_2 = 25 \text{ pN nm}^{-1}$  and decreasing the magnetic volume susceptibility to  $\kappa_1 \rightarrow \kappa_2 = 0.005$ . The resulting histograms of the particle positions, shown in the right panel of Fig. 4(b), confirm that for these new parameters the bistability is recovered even for a larger field of  $B = 25\text{mT}$ . Thus, for the latter system, we obtain the value of  $\bar{\chi} \sim 0.7$  at the largest field which is in the ballpark of our estimate  $\bar{\chi} = 0.8$  based on a single plaquette. Note that Fig. 4(a) shows an alternation of sign among many nearest neighboring plaquettes. However, the lattice of the pentagonal plaquettes is not bipartite, and thus frustrates the anti alignment of the plaquettes. A configuration in which all the neighboring plaquettes have opposite chirality (e.g., the check board pattern observed for the square spin ice system [56]) is geometrically impossible which suggests that the system has, at least, a disordered landscape of low energy states. As Figure 4(a) suggests, the configuration corresponds to an antiferrotoroid. Moreover, we have check that also with the new numerical conditions ( $N_2, \xi_2, \kappa_2$ ) we observe the topological charge transfer similar to Fig. 3(b).

To answer the second question, concerning the mutual distribution of chiralities, we note that Fig. 4(a) shows a largely antiferrotoroidal arrangement. However, the lattice of the plaquettes is frustrated and therefore no full antiferrotoroidicity can exist. We explore this angle by extracting the following nearest neighbor correlations:

$$\bar{\psi} = \frac{1}{N_{nn}} \sum_{\langle ij \rangle} \left(1 - \frac{\chi_i \chi_j}{|\chi_i \chi_j|}\right) \frac{1}{2}; \quad \bar{\sigma} = \frac{1}{N_{nn}} \sum_{\langle ij \rangle} \frac{\chi_i \chi_j}{\bar{\chi}}; \quad (4)$$

where the sum is performed over the  $N_{nn}$  nearest neighboring plaquettes. Both correlations counts how many links among nearest neighboring plaquettes are antiferrotoroidal, regardless of the intensity of the chiralities of the plaquettes. If all the nearest neighboring plaquettes were antiferrotoroidal (which is impossible because of the frustration of the lattice of the plaquettes) then  $\bar{\psi}$  would be equal to 1, and  $\bar{\sigma} \rightarrow -1$ .

We plot  $\bar{\psi}$  and  $\bar{\sigma}$  in Figs. 4(d,e). In the left images, both correlations show similar trends between experiments and numerical simulations. For the large system size (right images)  $\bar{\psi}$  increases steadily with the field reaching 0.68: almost the 68% of the links

are anti-ferromagnetic, namely 3.5 over 5 nearest neighbors. This results also reflects the arrangement of the toroidal moments shown in Fig. 4(a) for  $B = 25$  mT, where the system organizes in a lattice of full chiral cells placed in an alternating order. These results allow to characterize the disorder of the strongly coupled state of the Cairo ice in terms of plaquette chirality as a frustrated antiferrotoroid. The charge transfer prevents all plaquettes from reaching maximum chirality, while the the lattice of the plaquettes frustrates antiferrotoroidicity, preventing order.

## 6. Conclusions

We have investigated the arrangement of repulsive magnetic colloids confined in a lattice of double wells in the Cairo geometry. To experimentally realize such structure we have modified the lithographic process and developed a novel technique to trap absorbing magnetic particles using an optical ring. This strategy could be extended to other works aiming at trapping light-adsorbing magnetic particles to avoid undesired heating effects. We have observed that the Cairo ice breaks the ice rule as predicted for mixed coordination geometries, however, it does so with an inversion of the net charge transfer with respect to a previous experimental realization [32]. Moreover we have characterized this novel ensemble but looking at the effective toroidal moment associated to each pentagonal plaquette. We have found that the strongly coupled ensembled of the Cairo colloidal ice is a massively degenerate antiferroid.

Further extensions of our work include investigating the transition from Shakti to Cairo (ongoing) or using different size of particles to investigate hysteresis and memory effects [27, 35] that could emerge when the particles localize above the double wells [57]. Finally, it will be also interesting to investigate how the topological charges freeze or move after long time and the presence of aging of topological defects in our system. This will require longer observation time, beyond our current experimental capabilities, and thus could be a challenge for future work.

This project has received funding from the European Research Council (ERC) under the European Union’s Horizon 2020 research and innovation programme (grant agreement no. 811234). P. T. acknowledge support the Generalitat de Catalunya under Program “ICREA Acadèmia”. The work of Cristiano Nisoli was carried out under the auspices of the U.S. DoE through the Los Alamos National Laboratory, operated by Triad National Security, LLC (Contract No. 892333218NCA000001).

## References

- [1] O’Keeffe M and Hyde B G 1980 *Proc. R. Soc. Lond. A.* **295** 553–618
- [2] Shen Y and wang Q 2022 *Phys. Rep.* **964** 1–42
- [3] Macmillan R H 1979 *The Mathematical Gazette* **63** 251–255
- [4] Ressouche E, Simonet V, Canals B, Gospodinov M and Skumryev V 2009 *Phys. Rev. Lett.* **103**(26) 267204

- [5] Abakumov A M, Batuk D, Tsirlin A A, Prescher C, Dubrovinsky L, Sheptyakov D V, Schnelle W, Hadermann J and Van Tendeloo G 2013 *Phys. Rev. B* **87**(2) 024423
- [6] Urumov V 2002 *J. Phys. A: Math. Gen.* **35** 7317
- [7] Ralko A 2011 *Phys. Rev. B* **84**(18) 184434
- [8] Rojas M, Rojas O and de Souza S M 2012 *Phys. Rev. E* **86**(5) 051116
- [9] Rousochatzakis I, Läuchli A M and Moessner R 2012 *Phys. Rev. B* **85**(10) 104415
- [10] Wang R F, Nisoli C, Freitas R S, Li J, McConville W, Cooley B J, Lund M S, Samarth N, Leighton C, Crespi V H and Schiffer P 2006 *Nature* **439** 303–306
- [11] Nisoli C, Moessner R and Schiffer P 2013 *Rev. Mod. Phys.* **85**(4) 1473–1490
- [12] Skjærvø S H, Marrows C H, Stamps R L and Heyderman L J 2020 *Nat. Rev. Phys.* **2** 13–28
- [13] Mól L A S, Moura-Melo W A and Pereira A R 2010 *Phys. Rev. B* **82**(5) 054434
- [14] Rougemaille N, Montaigne F, Canals B, Duluard A, Lacour D, Hehn M, Belkhou R, Fruchart O, El Moussaoui S, Bendounan A and Maccherozzi F 2011 *Phys. Rev. Lett.* **106** 057209 ISSN 0031-9007
- [15] Zhang S, Gilbert I, Nisoli C, Chern G W, Erickson M J, O’Brien L, Leighton C, Lammert P E, Crespi V H and Schiffer P 2013 *Nature* **500** 553–557
- [16] Gilbert I, Chern G W, Zhang S, O’Brien L, Fore B, Nisoli C and Schiffer P 2014 *Nature Physics* **10** 670–675
- [17] Perrin Y, Canals B and Rougemaille N 2016 *Nature* **540** 410–413
- [18] Canals B, Chioar I A, Nguyen V D, Hehn M, Lacour D, Montaigne F, Locatelli A, Mentş T O, Burgos B S and Rougemaille N 2016 *Nat. Commun.* **7** 11446 ISSN 2041-1723
- [19] Vedmedenko E Y 2016 *Phys. Rev. Lett.* **116**(7) 077202
- [20] 2016 *Science* **352** 962–966 ISSN 0036-8075
- [21] Saccone M, Hofhuis K, Huang Y L, Dhuey S, Chen Z, Scholl A, Chopdekar R V, van Dijken S and Farhan A 2019 *Phys. Rev. Mater.* **3**(10) 104402
- [22] Makarova K, Strongin V, Titovets I, Syrov A, Zinchenko I, Samoylov V, Hofhuis K, Saccone M, Makarov A, Farhan A and Nefedev K 2021 *Phys. Rev. E* **103**(4) 042129
- [23] Shevchenko Y, Strongin V, Kapitan V, Soldatov K, Makarov A, Padalko M, Volotovskii R and Nefedev K 2022 *Phys. Rev. E* **106**(6) 064105
- [24] Merrigan C, Shohat D, Sirote C, Lahini Y, Nisoli C and Shokef Y 2022 preprint arXiv:2204.04000
- [25] Libál A, Reichhardt C and Reichhardt C J O 2006 *Phys. Rev. Lett.* **97**(22) 228302
- [26] Ortiz-Ambriz A, Nisoli C, Reichhardt C, Reichhardt C J O and Tierno P 2019 *Rev. Mod. Phys.* **91**(4) 041003

- [27] Libál A, Reichhardt C and Olson Reichhardt C J 2012 *Phys. Rev. E* **86**(2) 021406
- [28] Ortiz-Ambriz A and Tierno P 2016 *Nat Commun* **7** 10575 ISSN 2041-1723
- [29] Loehr J, Ortiz-Ambriz A and Tierno P 2016 *Phys. Rev. Lett.* **117**(16) 168001
- [30] Oğuz E C, Ortiz-Ambriz A, Shem-Tov H, Babià-Soler E, Tierno P and Shokef Y 2020 *Phys. Rev. Lett.* **124** 238003
- [31] Nisoli C 2014 *New J. Phys.* **16** 113049
- [32] Libál A, Lee D Y, Ortiz-Ambriz A, Reichhardt C, Reichhardt C J O, Tierno P and Nisoli C 2018 *Nat. Comm.* **9** 4146
- [33] Nisoli C 2018 *Phys. Rev. Lett.* **120** 167205
- [34] Libál A, Nisoli C, Reichhardt C and Reichhardt C J O 2017 *Sci. Rep.* **7** 651
- [35] Rodríguez-Gallo C, Ortiz-Ambriz A and Tierno P 2021 *Phys. Rev. Lett.* **126**(18) 188001
- [36] Han Y, Shokef Y, Alsayed A M, Yunker P, Lubensky T C and Yodh A G 2008 *Nature* **456** 898–903 ISSN 0028-0836
- [37] Shokef Y, Souslov A and Lubensky T C 2011 *Proc. Natl. Acad. Sci.* **108** 11804–11809 ISSN 0027-8424
- [38] Shokef Y, Han Y, Souslov A, Yodh A G and Lubensky T C 2013 *Soft Matter* **9** 6565–6570 ISSN 1744683X
- [39] Zhou D, Wang F, Li B, Lou X and Han Y 2017 *Phys. Rev. X* **7**(2) 021030
- [40] Leoni F and Shokef Y 2017 *Phys. Rev. Lett.* **118**(21) 218002
- [41] Kang S H, Shan S, Noorduyn W L, Khan M and J Aizenberg K B 2013 *Adv. Mater.* **25** 3380–3385
- [42] Coulais C, Teomy E, de Reus K, Shokef Y and van Hecke M 2016 *Nature* **535** 529–532
- [43] Meeussen A S, Oguz E C, Shokef Y and van Hecke M 2020 *Nat. Phys.* **16** 307–311
- [44] Li S, Deng B, Grinthal A, Schneider-Yamamura A, Kang J, Martens R S, Zhang C T, Li J, Yu S, Bertoldi K and Aizenberg J 2021 *Nature* **592** 386–391
- [45] Merrigan C, Nisoli C and Shokef Y 2021 *Phys. Rev. Res.* **3**(2) 023174
- [46] Meng Z, Liu M, Yan H, Genin G M and Chen C Q 2022 *Sci. Adv.* **8** eabn5460
- [47] Libál A, Reichhardt C J O and Reichhardt C 2009 *Phys. Rev. Lett.* **102**(23) 237004
- [48] Latimer M L, Berdiyrov G R, Xiao Z L, Peeters F M and Kwok W K 2013 *Phys. Rev. Lett.* **111**(6) 067001
- [49] Ma F, Reichhardt C, Gan W, Reichhardt C J O and Lew W S 2016 *Phys. Rev. B* **94**(14) 144405
- [50] Duzgun A and Nisoli C 2021 *Phys. Rev. Lett.* **126**(4) 047801
- [51] Mellado P, Concha A and Mahadevan L 2012 *Phys. Rev. Lett.* **109**(25) 257203
- [52] Mellado P, Concha A, Hofhuis K and Tapia I 2023 *Sci. Rep.* **13** 1245

- [53] Libál A, Nisoli C, Reichhardt C J O and Reichhardt C 2018 *Phys. Rev. Lett.* **120**(2) 027204
- [54] Le Cunuder A, Frérot I, Ortiz-Ambriz A and Tierno P 2019 *Phys. Rev. B* **99**(14) 140405
- [55] Lee D Y and Tierno P 2018 *Phys. Rev. Mater.* **2**(11) 112601
- [56] Morgan J P, Stein A, Langridge S and Marrows C H 2011 *Nat. Physics* **7** 75–79
- [57] Rodríguez-Gallo C, Ortiz-Ambriz A and Tierno P 2021 *Phys. Rev. Res.* **3**(4) 043023